

Hand-Aware Egocentric Motion Reconstruction with Sequence-Level Context

Kyungwon Cho Hanbyul Joo
 Seoul National University
 {cscandkswon, hb.joo}@snu.ac.kr

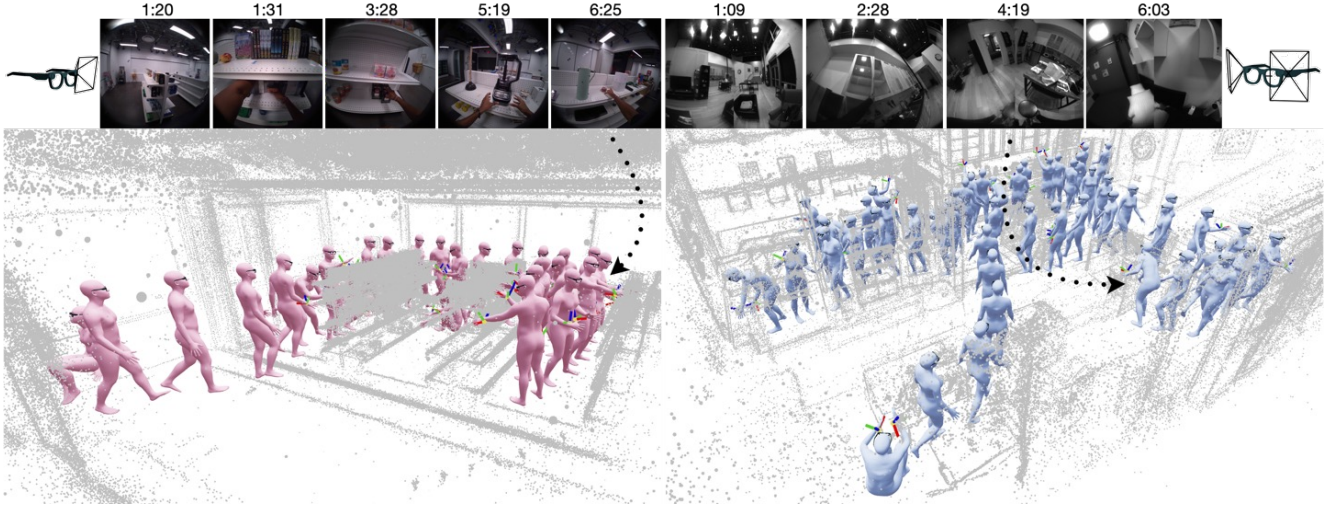


Figure 1. **HaMoS**. We present the first hand-aware, sequence-level diffusion framework that directly conditions on both head trajectory and intermittently visible hand cues caused by field-of-view limitations and occlusions, as in real-world egocentric devices.

Abstract

Egocentric vision systems are becoming widely available, creating new opportunities for human-computer interaction. A core challenge is estimating the wearer’s full-body motion from first-person videos, which is crucial for understanding human behavior. However, this task is difficult since most body parts are invisible from the egocentric view. Prior approaches mainly rely on head trajectories, leading to ambiguity, or assume continuously tracked hands, which is unrealistic for lightweight egocentric devices. In this work, we present **HaMoS**, the first hand-aware, sequence-level diffusion framework that directly conditions on both head trajectory and intermittently visible hand cues caused by field-of-view limitations and occlusions, as in real-world egocentric devices. To overcome the lack of datasets pairing diverse camera views with human motion, we introduce a novel augmentation method that models such real-world conditions. We also demonstrate that sequence-level contexts such as body shape and field-of-view are crucial for accu-

rate motion reconstruction, and thus employ local attention to infer long sequences efficiently. Experiments on public benchmarks show that our method achieves state-of-the-art accuracy and temporal smoothness, demonstrating a practical step toward reliable in-the-wild egocentric 3D motion understanding.

1. Introduction

Egocentric vision systems are becoming commercially available [1, 2, 4, 5], and it is expected that they will soon become part of everyday life. To enable effective human-computer interaction, these systems must be able to understand human motion and behavior in 3D. However, estimating full-body 3D human motion from an egocentric camera remains a highly challenging problem, since large portions of the user’s body are rarely visible from the first-person viewpoint. Recent approaches [20, 30, 32, 38, 53] leverage head trajectories as a proxy for body motion, demonstrating strong

correlations between head movement and body motions. However, head-only cues leave many motions fundamentally ambiguous, as multiple plausible 3D poses can correspond to nearly identical head trajectories.

Hand cues visible in egocentric videos play a crucial role in resolving such ambiguities. When hands are visible, their positions and movements provide direct evidence about body configurations. Even when hands are not visible, their absence serves as an informative cue about possible poses. However, existing approaches treat these cues as auxiliary signals for post-hoc optimization [30, 53]. It is computationally expensive and often results in unnatural motion. Accurately estimating human height provides another critical cue. Height constrains the range of plausible motions, because changes in vertical head position can imply different actions for people of different heights or body proportions. For example, a low head position for a tall individual is more likely to indicate sitting, while an identical head height for a shorter individual may correspond to standing or bending. Despite the importance of height and shape consistency, existing methods often fail to estimate stable body shape and instead rely on a fixed mean shape [11, 20, 27, 30, 32] or per-frame predictions that vary over time [38, 53].

In this paper, we present a hand-aware egocentric 3D human motion capture framework that directly incorporates hand cues and sequence-level context into the learning pipeline, removing the need for inefficient post-processing. Fully leveraging hand cues is challenging, because they are only partially observable due to limited fields of view, occlusions, and occasional tracking failures. The model is required to implicitly infer the field of view of the capturing device, since the absence of visible hands often indicates that the hands have moved outside the camera’s view. To address the lack of datasets that explicitly encode these visibility patterns, we introduce a hand visibility augmentation model that simulates out-of-view and occluded hand conditions. We leverage this technique with our new architecture designed to efficiently process intermittent hand cues and incorporate them into the motion reconstruction process. By utilizing both visible and invisible hand signals together with sequence-level information, our model resolves key motion ambiguities showing more accurate motion reconstructions. Furthermore, in contrast to previous approaches that rely on short temporal windows, our framework is designed to operate on full sequence-level inputs. This long-range temporal reasoning is particularly important for accurately predicting human height and body proportions, because height can be inferred more reliably when the model observes periods in which the user is standing still or walking. Via thorough evaluations, we demonstrate that our approach achieves state-of-the-art accuracy and temporal plausibility compared to existing methods.

Our main contributions are summarized as follows: (1) A

hand-aware diffusion model that integrates sparse hand cues directly into the generative process, creating an egocentric-aware motion prior that improves reconstruction accuracy in ambiguous scenarios; (2) Sequence-level context modeling by presenting a transformer-based encoder-decoder with local sliding-window attention; and (3) a novel and flexible hand visibility augmentation strategy that enables generalization to diverse egocentric cameras.

2. Related Work

Motion Capture from Body-Mounted Sensors or VR-Devices. Wearable motion capture using IMU sensors provides a camera-free alternative [3, 6], but lightweight systems with fewer sensors [22, 29, 30, 49, 54–57] often require global localization cues from head-mounted cameras [19, 30, 56] to address the inherent root drift from integration errors. Another related direction leverages VR/AR headsets, which provide 6-DoF (degrees of freedom) tracking for both the head and hand-held controllers (or wrists), often referred to as *three-point tracking*. These methods range from optimization-based approaches [14, 27, 28] to recent generative diffusion models [8, 11, 16] designed to handle the high uncertainty of this task, especially for lower-body motion. Unlike IMUs, these systems utilize accurate 6-DoF positional cues, providing strong upper-body constraints and reducing ambiguity in full-body motion estimation.

Motion Capture from Egocentric Videos. There has been growing interest in capturing 3D human body pose from body-worn cameras for their ability to record self-motion anywhere without third-person observations. Early approaches used impractical, downward-facing fisheye cameras to maximize body capture, but suffered from severe lens distortions [26, 46, 47, 50–52]. More recent studies address egocentric motion capture using frontal-facing cameras, either chest-mounted [25] or head-mounted [34, 37, 58, 59]. Closest to our setting are purely vision-based egocentric approaches using glasses-style devices (e.g., Meta Aria [1, 2]) [32, 38, 53]. Specifically, UniEgoMotion [38] employs a DINO-based image encoder, HMD-Square [20] adopts a CLIP encoder for RGB input combined with a voxel autoencoder for point-cloud processing, EgoEgo [32] relies solely on head trajectory as input, and EgoAllo [53] incorporates both head trajectories and sparse hand observations.

Generative Priors and Temporal Modeling. Our work builds on the dominant paradigm of diffusion models, which act as powerful generative priors for high-fidelity motion synthesis [13, 24, 45, 60]. While powerful, these models, especially when applied to reconstruction [11, 16], often inherit the limitations of standard transformers: they are confined to short temporal windows due to $O(N^2)$ attention complexity. To address this, long-sequence models [9, 33] are adopting efficient linear-complexity architectures, such as sliding-window attention, to capture long-range dependencies.

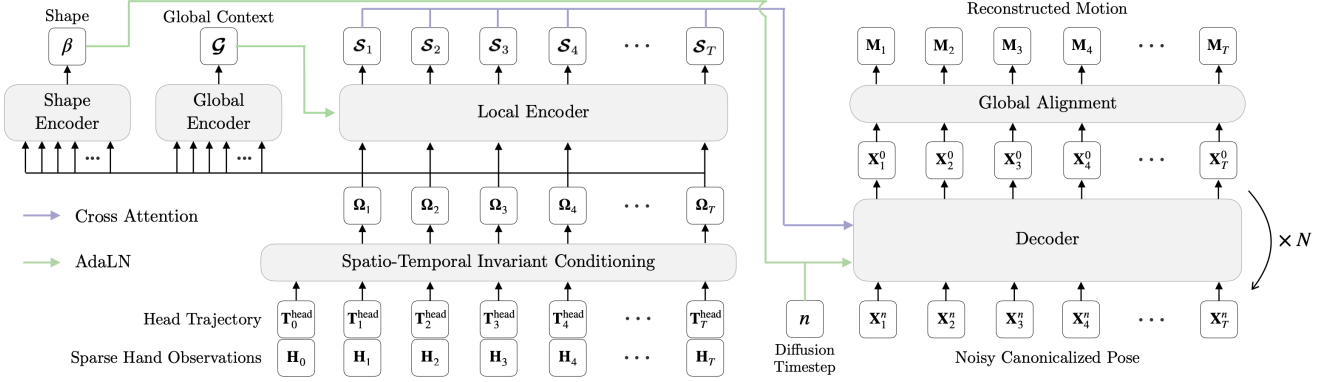


Figure 2. **Overview of Our Model.** The model \mathcal{F} takes the head trajectory $\mathbf{T}_{0:T}^{\text{head}}$ and sparse hand observations $\mathbf{H}_{0:T}$, which are first converted into spatio-temporally invariant conditioning features $\Omega_{1:T}$. The encoder \mathcal{E} processes $\Omega_{1:T}$ to predict a single body shape β and per-frame summary features $\mathcal{S}_{1:T}$. A diffusion decoder \mathcal{D} then conditions on these features to denoise a noisy canonicalized pose $\mathbf{X}_{1:T}^n$ and, via global alignment, reconstruct the full-body motion $\mathbf{M}_{1:T}$.

cies. Following this direction, our work employs a sliding-window attention mechanism for efficient sequence-level motion reconstruction.

3. Method

3.1. Problem Formulation

Given an egocentric video input, our goal is to reconstruct the wearer’s 3D full-body motion. Let $\mathbf{I}_{0:T} = \{I_t \in \mathbb{R}^{H \times W \times C}\}_{t=0}^T$ denote the egocentric image stream. From \mathbf{I} , we compute the head poses $\mathbf{T}_{0:T}^{\text{head}} = \{\mathbf{T}_t^{\text{head}} \in \text{SE}(3)\}_{t=0}^T$ defined in world coordinates and sparse wrist 6D pose observations $\mathbf{H}_{0:T} = \{\mathbf{H}_t^{\text{LHand}}, \mathbf{H}_t^{\text{RHand}}\}_{t=0}^T$. Here, each $\mathbf{H}_t^{\text{LHand/RHand}} = (\mathbf{T}_t^{\text{LHand/RHand}}, v_t^{\text{LHand/RHand}})$, where $\mathbf{T}_t^{\text{LHand/RHand}} \in \text{SE}(3)$ is its 6-DoF pose defined in the head coordinates and $v_t^{\text{LHand/RHand}} \in \{0, 1\}$ is its binary visibility state. A non-visible state can occur due to occlusion, motion blur, or the wrist moving outside of camera’s field of view (FoV). Our model \mathcal{F} , *HaMoS*, takes $\mathbf{T}_{0:T}^{\text{head}}$ and $\mathbf{H}_{0:T}$ as input, and produces the reconstructed human motion $\mathbf{M}_{1:T}$ as output:

$$\mathbf{M}_{1:T} = \mathcal{F}(\mathbf{T}_{0:T}^{\text{head}}, \mathbf{H}_{0:T}), \quad (1)$$

where $\mathbf{M}_{1:T} = \{\beta, \mathbf{r}_{1:T}, \Phi_{1:T}, \Theta_{1:T}\}$ is in SMPL format [42] with the shape parameter $\beta \in \mathbb{R}^{16}$, root translation $\mathbf{r}_{1:T} = \{r_t \in \mathbb{R}^3\}_{t=1}^T$, root orientation $\Phi_{1:T} = \{\phi_t \in \text{SO}(3)\}_{t=1}^T$, $\Theta_{1:T} = \{\theta_t = (\theta_t^1, \dots, \theta_t^{J-1}); \theta_t^j \in \text{SO}(3)\}_{t=1}^T$ are the joint angles, where J is the number of body joints in SMPL. The root poses are defined in the world coordinate system, consistent with \mathbf{T}^{head} . Note that we predict a single shape β for a whole sequence, contrasting prior approaches that use a fixed mean shape [27, 30, 32] or per-frame shape [38, 53]. We implement our model \mathcal{F} via a transformer-based diffusion architecture [21, 39], which progressively denoises the motion \mathbf{M} conditioned on the sparse cues from the head trajectory \mathbf{T}^{head} and the detected hand

cues \mathbf{H} . See Fig. 2 for an overview of our framework.

3.2. Preprocessing and representation

Preprocessing. Given the egocentric images \mathbf{I} , we first compute camera poses $\mathbf{T}_t^{\text{cam}} \in \text{SE}(3)$ ¹ via off-the-shelf SLAMs or SfMs. We define a world coordinate system where the z -axis aligns with gravity and the floor is at $z = 0$. Since the camera and head joints are not co-located, we compute the head poses as $\mathbf{T}_t^{\text{head}} = \mathbf{T}^{\text{cam} \rightarrow \text{head}} \mathbf{T}_t^{\text{cam}}$, where $\mathbf{T}^{\text{cam} \rightarrow \text{head}}$ is a pre-computed rigid transformation from the *camera coordinate* to the *head coordinate* based on a mean body shape. We observe $\mathbf{T}^{\text{cam} \rightarrow \text{head}}$ is negligibly affected by variations in the shape parameter β . The 6D hand observations and visibility $\mathbf{H}_t^{\text{Hand}}$ are also extracted using off-the-shelf hand pose estimation modules. For Aria [17], we use the internal Aria software tools to compute $\mathbf{T}_t^{\text{cam}}$ and $\mathbf{H}_t^{\text{hand}}$.

Coordinate and Representation. Learning full-body motion from long, sparse signal sequences end-to-end requires spatio-temporally invariant conditioning. To this end, we convert the raw signals $(\mathbf{T}_t^{\text{head}}, \mathbf{H}_t^{\text{LHand}}, \mathbf{H}_t^{\text{RHand}})$ into a normalized representation that is invariant to both spatial and temporal variations.

For the head trajectory, we follow the previous work [53], by defining the per-frame canonical frame at the head’s floor projection, with its z -axis aligned with gravity and y -axis aligned to the forward direction of the head: $\mathbf{T}_t^{\text{cano} \rightarrow \text{world}}$. Specifically, the condition vector $\Omega_t \in \mathbb{R}^D$ is computed by a simple neural net function Γ as follows:

$$\Omega_t = \Gamma(\Delta \mathbf{T}_t^{\text{head}}, \mathbf{R}_t^{\text{head} \rightarrow \text{cano}}, h_t, \Delta \mathbf{R}_t^{\text{cano}}, \mathbf{T}_t^{\text{head} \rightarrow \text{head}}) \quad (2)$$

where $\Delta \mathbf{T}_t^{\text{head}}$ is the relative head pose from $t-1$, $\mathbf{R}_t^{\text{head} \rightarrow \text{cano}}$

¹ $\mathbf{T}_t^{\text{cam}}$ can be considered as the coordinate transformation from the camera coordinate to the world coordinate, which can be equivalently denoted as $\mathbf{T}_t^{\text{cam} \rightarrow \text{world}}$. Similarly, $\mathbf{T}_t^{\text{head}} = \mathbf{T}_t^{\text{head} \rightarrow \text{world}}$.

is the canonicalized head orientation, and h_t is the height of the head, extracted from $\mathbf{T}_t^{\text{head}}$. Unlike EgoAllo [53], we additionally include the relative rotation in the canonical coordinate $\Delta\mathbf{R}_t^{\text{cano}}$ from frame $t - 1$, since our model explicitly predicts the root orientation Φ , as discussed in the next section. We also newly introduce hand conditions $\mathbf{T}_t^{\text{hand} \rightarrow \text{head}} = (\mathbf{T}_t^{\text{lHand} \rightarrow \text{head}}, \mathbf{T}_t^{\text{rHand} \rightarrow \text{head}})$, representing the relative hand poses with respect to the head coordinate. When the hand is not visible (*i.e.* when $v_t^{\text{lHand/rHand}} = 0$), the corresponding cues are replaced with learnable null embeddings. Notably, we do not include temporal motion cues for the hands, as wrist observations are often intermittent.

Global Alignment. Similar to previous work [27, 28, 53], we leverage \mathbf{T}^{head} obtained from SLAM for global localization by directly deriving the root translation \mathbf{r}_t . However, unlike EgoAllo [53], we predict the relative root orientation $\mathbf{R}_t^{\text{root} \rightarrow \text{cano}}$ with respect to the canonical coordinate as the model output. Concretely, the final root orientation is computed as $\phi_t = \mathbf{R}_t^{\text{cano} \rightarrow \text{world}} \mathbf{R}_t^{\text{root} \rightarrow \text{cano}}$. We demonstrate that our representation provides an additional 3DoF in global orientation, leading to improved motion stability and accuracy.

3.3. Architecture

We adopt a conditional diffusion model [21] to learn a plausible motion distribution from the processed conditioning features, $\Omega_{1:T} = \{\Omega_t\}_{t=1}^T$. For the model’s architecture, we use an encoder-decoder transformer [48], which is well-suited for time-series data. To efficiently process arbitrarily long sequences, we implement both encoder \mathcal{E} and decoder \mathcal{D} using sliding window local attention with an attention horizon of W [9, 10, 23, 33] and Rotary Positional Embedding [44], which reduces the computational complexity from quadratic to linear.

Encoder. The encoder \mathcal{E} processes conditioning features $\Omega_{1:T}$ through three sub-components to produce the predicted shape parameter $\hat{\beta}$ and per-frame summaries $\mathcal{S}_{1:T}$:

$$\begin{aligned}\hat{\beta} &= \mathcal{E}_{\text{shape}}(\Omega_{1:T}) \in \mathbb{R}^{16} \\ \mathcal{G} &= \mathcal{E}_{\text{global}}(\Omega_{1:T}) \in \mathbb{R}^D \\ \mathcal{S}_{1:T} &= \mathcal{E}_{\text{local}}(\Omega_{1:T}, \mathcal{G}) \in \mathbb{R}^{T \times D}\end{aligned}\quad (3)$$

The sub-encoders $\mathcal{E}_{\text{shape}}$ and $\mathcal{E}_{\text{global}}$ capture sequence-level, frame-invariant representations, $\hat{\beta}$ and global context \mathcal{G} . We implement them with a few local attention transformer layers to first aggregate local cues, which are then fed into an attention-based pooling layer [31]. Importantly, shape cues need to be inferred from a global perspective, since human height can only be reliably estimated from specific frames (*e.g.*, upright postures), which are often ambiguous if observed within local temporal windows. This design choice marks a key distinction from prior work [53]. $\mathcal{E}_{\text{local}}$ produces summaries $\mathcal{S}_{1:T}$ by processing conditions $\Omega_{1:T}$

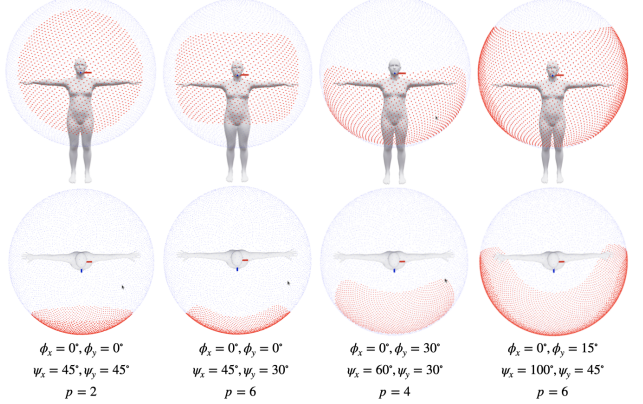


Figure 3. **Examples of our spatial augmentation method.** Red areas indicate the simulated FoV. Our method flexibly generates diverse and realistic egocentric FoVs by sampling parameters.

through locally attentive mechanisms that aggregate information across neighboring frames, enabling processing of long-term sequence-level input. To incorporate global cues, the global context \mathcal{G} is injected via AdaLN-Zero [39], enabling global modulation of the local aggregation process.

Decoder. The decoder \mathcal{D} does not directly denoise final motion \mathbf{M} . Instead, it denoises the canonicalized pose representation, denoted as $\mathbf{X}_{1:T}^0 = \{\mathbf{R}_{1:T}^{\text{root} \rightarrow \text{cano}}, \Theta_{1:T}\}$. The root translation \mathbf{r} and orientation Φ are then computed as described in the Global Alignment section. This decoder \mathcal{D} is implemented as a DiT architecture [39], conditioned on the encoded summary feature $\mathcal{S}_{1:T}$ and body shape $\hat{\beta}$:

$$\hat{\mathbf{X}}_{1:T}^0 = \mathcal{D}(\mathbf{X}_{1:T}^n, n, \hat{\beta}, \mathcal{S}_{1:T}), \quad (4)$$

where $n \in [1, N]$ is the diffusion timestep and $\hat{\mathbf{X}}_{1:T}^0$ is the predicted $\mathbf{X}_{1:T}^0$. The noised input $\mathbf{X}_{1:T}^n$ is defined by the DDPM [21] forward process $q(\mathbf{X}_{1:T}^n | \mathbf{X}_{1:T}^0) = \mathcal{N}(\mathbf{X}_{1:T}^n; \sqrt{\bar{\alpha}_n} \mathbf{X}_{1:T}^0, (1 - \bar{\alpha}_n) \mathbf{I})$, where $\bar{\alpha}_n$ is the noise schedule. We inject global conditions n and $\hat{\beta}$ via AdaLN, while the per-frame summary $\mathcal{S}_{1:T}$ is injected via cross-attention, using a local attention mask.

3.4. Training

Hand Visibility Augmentation. Training egocentric motion models is challenging, as large-scale datasets pairing egocentric video with body annotations are scarce and often device-restricted [18, 35]. Our goal is to develop a device-agnostic general model. To overcome the data bottleneck, we leverage the AMASS [36] dataset and realistically simulate sparse hand visibilities by applying a novel two-stage augmentation: spatial and temporal.

For spatial augmentation, we aim to simulate real-world FoV complexities like camera tilt, varying aspect ratios, lens masks, and distortions, which are often simplified in ideal

pinhole models [12, 28]. We propose a flexible model to simulate these effects. We first compute the wrist’s yaw ψ_x and pitch ψ_y in head coordinates. We then define the FoV using five parameters: center offset (ϕ_x, ϕ_y) for tilt, half-angles (γ_x, γ_y) for FoV size and aspect ratio, and a power p for lens distortion and shape. A wrist is visible when its angles satisfy the following generalized ellipse equation:

$$\left| \frac{\psi_x - \phi_x}{\gamma_x} \right|^p + \left| \frac{\psi_y - \phi_y}{\gamma_y} \right|^p \leq 1 \quad (5)$$

By sampling these parameters from realistic distributions during training, we expose the model to diverse conditions, improving its generalization. (See Fig. 3 for examples)

For temporal augmentation, we mimic realistic short-term (e.g., motion blur) and long-duration drops (e.g., occlusion), instead of simple random masking [7]. To achieve this, we propose a two-stage stochastic process. First, to control the overall drop rate, the number of drop events is sampled from a Poisson distribution. Then the length of each event is drawn from a Log-Normal distribution, modeling the heavy-tailed nature of real-world occlusions.

Loss Functions. We train our model with a total objective \mathcal{L} , combining $\mathcal{L}_{\text{simple}}$, $\mathcal{L}_{\text{shape}}$ and \mathcal{L}_{aux} :

$$\mathcal{L} = \mathcal{L}_{\text{simple}} + \lambda_{\text{shape}} \mathcal{L}_{\text{shape}} + \mathcal{L}_{\text{aux}} \quad (6)$$

$\mathcal{L}_{\text{simple}}$ is the standard DDPM [21] objective:

$$\mathcal{L}_{\text{simple}} = \mathbb{E}_{n, \mathbf{X}^0, \Omega} [\|\mathbf{X}^0 - \hat{\mathbf{X}}^0\|^2] \quad (7)$$

$\mathcal{L}_{\text{shape}}$ enforces the shape consistency. Instead of a direct loss on the raw β , which are PCA-derived and not physically meaningful, we minimize the 3D T-pose joint position error:

$$\mathcal{L}_{\text{shape}} = \|\text{FK}(\mathbf{0}, \beta) - \text{FK}(\mathbf{0}, \hat{\beta})\|^2 \quad (8)$$

, where FK is the forward kinematics function.

\mathcal{L}_{aux} regularizes motion to align with 3D physical constraints [45]. Let $\hat{\mathbf{M}}_{1:T}$ be the motion reconstructed from predicted $\hat{\mathbf{X}}_{1:T}^0$ and $\hat{\beta}$. \mathcal{L}_{aux} includes joint position loss \mathcal{L}_{pos} and foot skating loss $\mathcal{L}_{\text{skat}}$:

$$\begin{aligned} \mathcal{L}_{\text{pos}} &= \frac{1}{T} \sum_{t=1}^T \|\text{FK}(\mathbf{M}_t, \beta) - \text{FK}(\hat{\mathbf{M}}_t, \hat{\beta})\|^2 \\ \mathcal{L}_{\text{skat}} &= \frac{1}{T-1} \sum_{t=1}^{T-1} \|\text{FK}(\hat{\mathbf{M}}_{t+1}, \hat{\beta}) - \text{FK}(\hat{\mathbf{M}}_t, \hat{\beta})\|^2 \cdot c_t \end{aligned} \quad (9)$$

, where c_t is the ground-truth binary contact label. These losses are scaled by $\bar{\alpha}_n$ to enforce physical accuracy primarily when the signal level is high:

$$\mathcal{L}_{\text{aux}} = \bar{\alpha}_n (\lambda_{\text{pos}} \mathcal{L}_{\text{pos}} + \lambda_{\text{skat}} \mathcal{L}_{\text{skat}}) \quad (10)$$

We find that \mathcal{L}_{aux} is crucial for satisfying the hand condition \mathbf{H} and generating stable motion.

3.5. Inference

We use DDIM [43] sampling for motion generation. While the feed-forward denoiser’s prediction is accurate, we integrate test-time guidance optimization at each sampling step to better satisfy the sparse hand constraints \mathbf{H} . The objective is to find a refined motion $\tilde{\mathbf{M}}^0$ by minimizing \mathcal{L}_{opt} :

$$\begin{aligned} \mathcal{L}_{\text{opt}} = \sum_{t=1}^T \sum_{j \in \{\text{lHand}, \text{rHand}\}} & \left[\bar{\alpha}_n \|\text{FK}_j(\tilde{\mathbf{M}}_t^0, \hat{\beta}) - \text{FK}_j(\hat{\mathbf{M}}_t^0, \hat{\beta})\|^2 \right. \\ & \left. + s \cdot v_t^j \cdot (1 - \bar{\alpha}_n) \|\text{FK}_j(\tilde{\mathbf{M}}_t^0, \hat{\beta}) - p_t^j\|^2 \right] \end{aligned} \quad (11)$$

, where FK_j denotes joint j ’s position, p_t^j is the observed wrist position in world coordinates derived from \mathbf{H} , and s is the guidance scale. We optimize only the arm joints [27]. The objective balances two terms. The first term (prior term) acts as a regularizer, using the denoiser’s prior to ensure motion plausibility. The second term (constraint term) acts as a perturbation, pulling the wrist toward the target p_t^j . This dynamically leverages \mathcal{D} ’s denoising ability, as the constraint dominates in early steps, while the prior dominates in late steps, ensuring the motion remains on the motion manifold. This frame-independent guidance is highly parallelizable, avoiding slow post-hoc optimization.

4. Experiments

4.1. Experiment Setting

Dataset. We use the AMASS [36] dataset for training and simulated evaluation. Sequences are resampled to 30fps and preprocessed following HuMoR [41], adjusting the floor and annotating foot contact labels. We train on the AMASS train split with stochastic augmentation (Sec. 3.4). We evaluate on AMASS validation and test splits. For real-world evaluation, we use EgoExo4D [18] validation set, annotating hand observations \mathbf{H} via the Aria MPS services, retaining tracks with confidence higher than 90%.

Implementation Details. We train using AdamW optimizer with a learning rate 10^{-4} , weight decay 10^{-4} , and a batch size of 32 for 16 hours on 8 A5000 GPUs. For diffusion, we set $N = 1000$ timesteps with a cosine noise schedule. Max training sequence length is 512 with attention horizon $W = \pm 63$, implemented via FlexAttention [15]. We use an EMA rate of 0.9999. Hyperparameters are $\lambda_{\text{shape}} = 2.0$, $\lambda_{\text{pos}} = 0.25$, $\lambda_{\text{skat}} = 0.4$, $s = 8.0$. Test-time optimization uses Theseus [40] Levenberg-Marquardt optimizer.

Metrics. We use Mean Per Joint Position Error (**MPJPE**, mm), Mean Per Joint Velocity Error (**MPJVE**, cm/s), and **Jerk** (km/s³) (the third derivative of position) to evaluate motion quality. To assess hand observations \mathbf{H} , we use Hand Position Error (**Hand PE**, mm) and Visible Hand Position

Method	MPJPE \downarrow	MPJVE \downarrow	Jerk \downarrow	Hand PE \downarrow	Vis Hand PE \downarrow	Height \downarrow	Span \downarrow	Height Std \downarrow	Span Std \downarrow	Runtime \downarrow
EgoAllo † (w/o opt)	122.99	44.02	0.350	318.69	298.01	3.80	6.24	1.87	2.43	2.39
EgoAllo † (w/ opt)	99.32	31.66	0.152	164.80	41.49	3.86	6.19	1.84	2.35	99.05
Ours (w/o opt)	81.35	25.81	0.117	146.71	56.98	2.40	4.61	0.0	0.0	2.01
Ours (w/ opt)	80.71	25.55	0.117	136.51	37.18	2.40	4.61	0.0	0.0	5.78

Table 1. **Quantitative Results on AMASS.** Comparison with EgoAllo on simulated sparse hand observation. w/o opt denotes evaluation without optimization; w/ opt denotes evaluation with optimization.

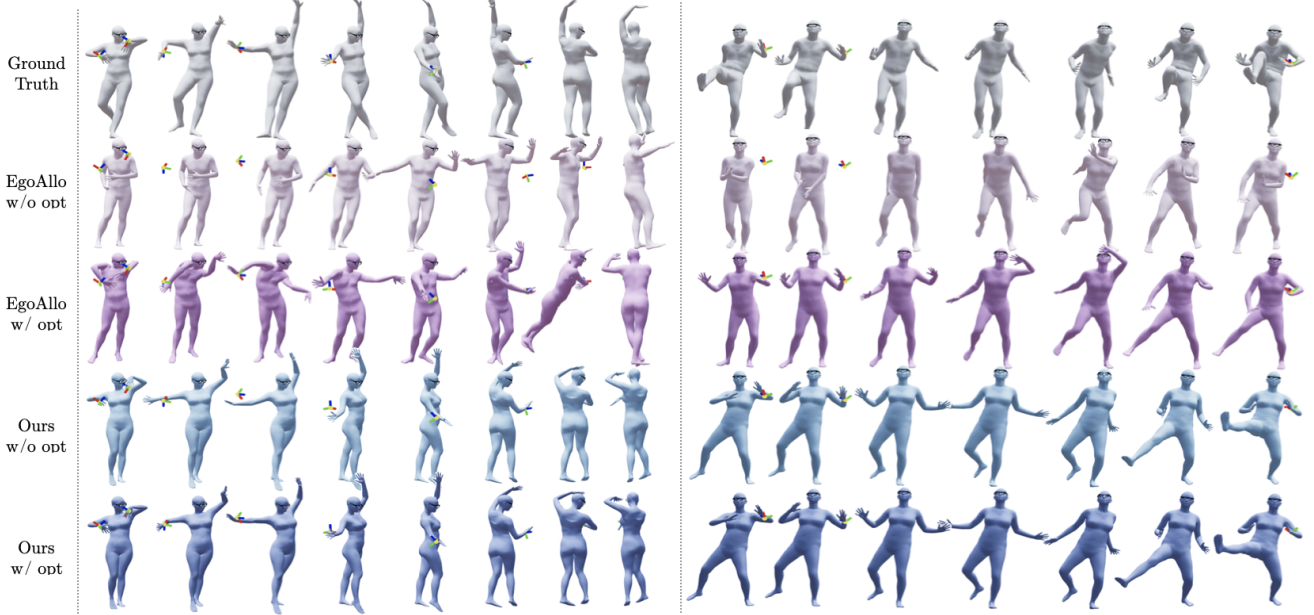


Figure 4. **Qualitative Results on AMASS.** **(Left)** In a dance sequence, EgoAllo (top) produces unnatural arm poses and unstable motion, while our model (bottom) remains plausible and smooth. **(Right)** During a kick, EgoAllo’s (top) prior incorrectly hallucinates the invisible arm back into FoV. Our egocentric-aware model (bottom) correctly predicts the arm moving outside the view.

Error (**Vis Hand PE**, mm, Hand PE on visible frames). For shape, we use **Height Error** (cm) and **Span Error** (cm) for accuracy and Height Standard Deviation (**Height Std**, cm) and Span Standard Deviation (**Span Std**, cm) for consistency. Height and Span are defined as the maximum vertical and horizontal vertex distances in a T-pose. **Runtime** (sec) measures the average execution time per sequence, inclusive of optimization setup on an RTX3090Ti GPU.

4.2. Comparison on Sparse Hand Observation

Baselines. We compare with EgoAllo [53], a method injecting hand conditions via guidance optimization. For evaluation on AMASS, we retrained EgoAllo using only the AMASS train set, matching our setup for fairness. We simulate sparse hand visibility using fixed, pre-generated augmentations (Sec. 3.4) for each sequence. For evaluation on EgoExo4D, we use the official pre-trained EgoAllo weights. For EgoAllo, we use the mean of its shape predictions for

all metrics except Height and Span Std.

Results. Table 1 shows that our method, in both its feed-forward and optimized versions, achieves clear improvement over the baseline across motion quality and shape accuracy and consistency. The key difference lies in constraint satisfaction. While our feed-forward Vis Hand PE trails EgoAllo’s optimized version, our overall Hand PE is superior. Our prior, conditioned on hand cues and egocentric-aware global context \mathcal{G} (containing FoV information), correctly places long-period invisible hands outside the FoV. In contrast, EgoAllo’s prior, conditioned only on head motion, hallucinates invisible hands back into the FoV (Fig. 4). Its optimization-based injection cannot fully correct this prior, which tends to revert to incorrect poses. This conflict causes the arm to snap to the observed position when visibility changes, resulting in implausible motion and increasing MPJVE and Jerk. Conversely, our encoder-decoder architecture propagates hand information effectively, ensuring a

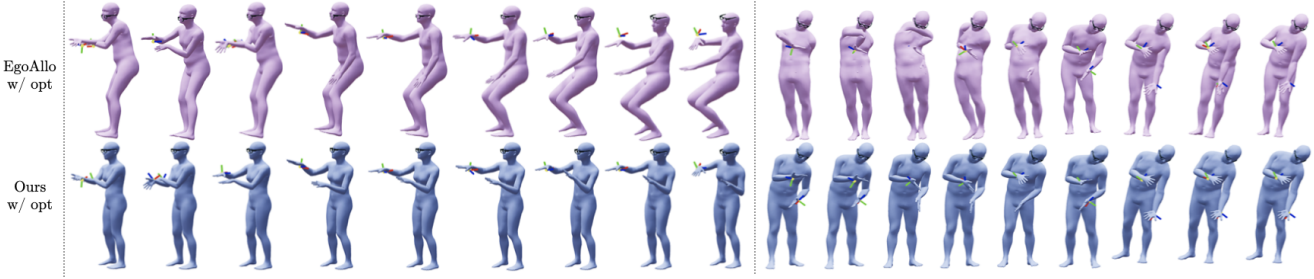


Figure 5. **Qualitative Results on EgoExo4D (Left)** In a cooking sequence, EgoAllo’s (top) severe shape inconsistency causes its pose to fluctuate between standing and sitting, even under static conditions. Our model (bottom) predicts a stable shape and consistent motion. **(Right)** During bike repair, EgoAllo’s (top) optimization produces unnatural poses, causing the arm to penetrate the torso and bend at impossible angles. Our model (bottom) maintains physical plausibility.

Method	Jerk \downarrow	Vis Hand PE \downarrow	Height Std \downarrow	Span Std \downarrow	Runtime \downarrow
EgoAllo (w/o opt)	0.110	298.4543	2.23	3.04	4.12
EgoAllo (w/ opt)	0.065	21.80	2.21	2.99	228.15
Ours (w/o opt)	0.048	51.24	0.0	0.0	2.22
Ours (w/ opt)	0.048	30.21	0.0	0.0	6.38

Table 2. **Quantitative Results on EgoExo4D.** Comparison on real-world data where motion ground truth is unavailable. w/o opt and w/ opt are defined as in Table 1.

smooth, plausible hand trajectory.

Our optimization method better maintains motion plausibility. Fig. 4 and Fig. 5 show EgoAllo’s optimization often moves off-manifold, leading to artifacts such as body penetration and physically implausible joint angles. In contrast, our optimization is a minimal, on-manifold refinement, relying on a strong prior. This prevents the generation of unnatural body poses, while still achieving the best hand accuracy. It is also over 17x faster and achieves superior smoothness, all without the explicit smoothness loss term that EgoAllo requires.

Our model’s single shape estimation approach yields a more accurate and consistent β . Table 1 shows EgoAllo’s predictions are non-unique and less accurate. We achieve this through our encoder’s attention-based pooling, which aggregates important cues from the entire sequence, while EgoAllo may dilute this information. This non-unique estimation also leads to a consistency problem. Fig. 5 shows EgoAllo can predict different motions (*e.g.*, a small person standing vs a large person sitting) under the same input conditions. Our model, by predicting a single, stable β , reduces this ambiguity and improves motion consistency.

On EgoExo4D (Table 2), our model produces smoother motion, while EgoAllo (w/ opt) achieves the best Vis Hand PE. We posit this is because EgoExo4D’s motion is more static than AMASS, making it easier to refine via aggressive post-optimization. Furthermore, EgoAllo’s shape consistency degrades on EgoExo4D compared to AMASS. This

Method	FoV	MPJPE \downarrow	MPJVE \downarrow	Hand PE \downarrow	Vis Hand PE \downarrow
EgoPoser $_{90}^{\dagger}$	90	121.17	39.88	173.61	110.58
EgoPoser $_{180}^{\dagger}$	90	143.98	48.53	298.25	96.50
EgoAllo † (w/o opt)	90	124.44	43.19	317.97	390.66
EgoAllo † (w/ opt)	90	113.80	34.41	244.97	45.67
Ours (w/o opt)	90	94.22	27.68	199.47	68.08
Ours (w/ opt)	90	93.58	27.48	194.24	41.78
EgoPoser $_{90}^{\dagger}$	180	117.85	37.79	153.70	128.65
EgoPoser $_{180}^{\dagger}$	180	105.33	34.43	96.38	77.80
EgoAllo † (w/o opt)	180	124.46	43.20	317.82	300.77
EgoAllo † (w/ opt)	180	90.67	28.28	99.22	42.21
Ours (w/o opt)	180	73.98	23.03	97.52	56.58
Ours (w/ opt)	180	73.09	22.58	82.20	36.59

Table 3. **Quantitative Results on HMD Setting.** Comparison with EgoPoser and EgoAllo on pinhole FoV assumption. The FoV indicates the test-time FoV setting.

instability can be observed in practice, as illustrated in the qualitative examples in Fig. 5.

4.3. Comparison on HMD Setting

Baselines. We compare with EgoPoser [28], also using FoV constraints, to demonstrate our generalizability. As EgoPoser requires a fixed FoV, we trained two specialist models on our train set: EgoPoser $_{90}^{\dagger}$ (trained only on 90° FoV) and EgoPoser $_{180}^{\dagger}$ (trained only on 180° FoV), both using a mean shape. We also include EgoAllo (Sec. 4.2) as a baseline. We evaluated all models using EgoPoser’s pinhole FoV method for hand masking and excluding temporal drops, which EgoPoser does not model, for fairness.

Results. Table 3 shows our single generalist model, untrained on specific FoVs, outperforms the specialists and EgoAllo. EgoPoser’s models fail to generalize on mismatched FoVs. When EgoPoser $_{180}^{\dagger}$ is tested on 90° data, its MPJPE increases by 22.81mm and Hand PE by 124.64mm and vice-versa. This suggests they overfit their training FoV, especially for hands. In contrast, our model handles both

Method	MPJPE \downarrow	MPJVE \downarrow	Jerk \downarrow	Hand PE \downarrow	Vis Hand PE \downarrow
No Shape/Global	97.06	25.17	0.104	161.25	79.70
No Shape Cond	86.55	26.59	0.111	156.09	65.05
No Global	83.53	26.82	0.116	152.73	65.99
Concat	81.60	26.13	0.112	149.92	61.42
No Auxiliary	83.44	27.56	0.163	153.17	60.57
No Root Ori	87.68	26.95	0.120	154.81	66.17
Head	82.13	25.43	0.119	148.71	58.17
Default	81.35	25.81	0.117	146.71	56.98

Table 4. **Quantitative Results on Ablation Studies.** Comparison of variants on simulated hand observation. All variants evaluated without optimization.

scenarios, achieving superior accuracy and smoothness. Our model better adheres to visible hand information, evidenced by its lower Vis Hand PE. Regarding Hand PE, which includes invisible hands, our performance is comparable on 180° data and slightly higher on 90° data. This is notable, as EgoPoser knew the exact FoV boundaries, while our model must infer them at test-time. Although our augmentation method (Sec. 3.4) does not produce an exact pinhole model, our model robustly generalizes to these unseen FoVs.

4.4. Ablation Studies

We conduct ablation studies to validate our key design choices, comparing our full model against variants with specific components removed.

Importance of Global Context. To demonstrate the necessity of our sequence-level context \mathcal{G} and β , we define four baselines: (1) **No Shape/Global** removes all sequence-level contexts, using mean shape; (2) **No Shape Cond** omits β as a condition in the decoder; (3) **No Global** predicts β but removes \mathcal{G} ; and (4) **Concat** injects \mathcal{G} via concatenation. First, removing all context ((1) **No Shape/Global**) degrades MPJPE to 97.06mm. Re-introducing $\mathcal{E}_{\text{shape}}$ ((3) **No Global**) improves this to 83.53mm, proving predicting an identity-preserving shape β is crucial for accurate motion reconstruction. The contribution of the global motion context \mathcal{G} is also critical. Adding \mathcal{G} via AdaLN (**Default**) improves overall MPJPE, but primarily hand accuracy, reducing both Hand PE and Vis Hand PE. This improvement supports our hypothesis: the sequence-level context \mathcal{G} is essential for generating hand trajectories consistent with the sequence-specific FoV. It achieves this by encoding the FoV boundaries from analyzing the spatial distribution of visibility transitions. By implicitly learning these visual limits, the model avoids implausible predictions, specifically resolving the ambiguity of hand locations that local cues cannot address. We also validate the injection strategy. The degradation in (2) **No Shape Cond** (81.35mm to 86.55mm) implies that the denoiser must be conditioned on body shape β , likely to predict

correct joint orientations for different bone lengths. Additionally, (4) **Concat** proves suboptimal. It fails to match the hand accuracy of AdaLN, suggesting simple concatenation is insufficient to effectively inject FoV information encoded in \mathcal{G} . This indicates AdaLN is more effective than simple concatenation for incorporating sequence-level context.

Auxiliary Loss. We validate the importance of auxiliary loss \mathcal{L}_{aux} . Although many diffusion models [11, 32, 38, 53] rely solely on $\mathcal{L}_{\text{simple}}$, which operates purely on joint orientations, we argue that this is insufficient. Small orientation errors accumulate along the kinematic chain, resulting in large position errors at end-effectors like hands. We introduce \mathcal{L}_{aux} to penalize 3D position errors. Comparing against (5) **No Auxiliary**, removing \mathcal{L}_{aux} degrades performance: MPJPE worsens (81.35mm to 83.44mm) and end-effector accuracy drops (Vis Hand PE 56.98mm to 60.57mm). This confirms \mathcal{L}_{aux} is critical for satisfying the hand condition **H**. It also acts as a 3D geometric regularizer; its removal causes a 39% spike in Jerk. Thus, \mathcal{L}_{aux} is important for generating accurate and smooth motion.

Root Representation. We validate our root orientation parameterization. The (6) **No Root Ori** variant, mimicking EgoAllo [53] by directly stitching predicted body to \mathbf{T}^{head} , performs worst. This approach removes 3DoF, making the body’s global orientation dependent on the head and offering no flexibility. The (7) **Head** variant predicts root orientation in head coordinate system ($\mathbf{R}_t^{\text{root} \rightarrow \text{head}}$). While this restores flexibility, it forces the model to learn a difficult 3D mapping relative to the volatile head coordinate. In contrast, our gravity-aligned canonical frame provides a stable 2D mapping that is easier to learn. This strikes the best balance between flexibility and stability, yielding top performance.

5. Discussion

We have presented a transformer-based diffusion framework for reconstructing full-body motion from head trajectories and sparse wrist observations at the sequence level. By predicting sequence-level context (\mathcal{G}), which captures FoV, and a single, consistent body shape (β), the model learns an egocentric-aware prior that reduces motion ambiguity and improves stability. Flexible camera augmentation enables generalization across diverse FoV configurations, and an optional lightweight optimization refines hand trajectories while preserving the plausibility of the learned motion prior.

While our framework is robust in practice, it depends on SLAM and hand-tracking modules, and rare catastrophic failures in these components can still degrade reconstruction. Our experiments also assume a flat ground plane and do not model detailed finger articulation. Improving robustness to such failures and relaxing these assumptions, for example by incorporating richer hand models and non-planar scene geometry, are promising directions for future work.

Hand-Aware Egocentric Motion Reconstruction with Sequence-Level Context

Supplementary Material

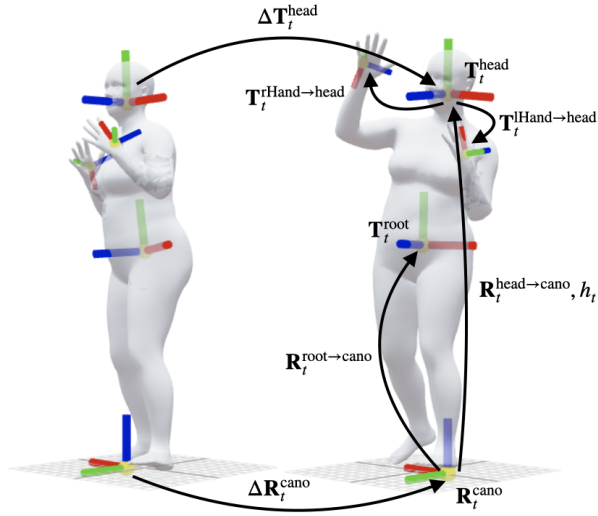


Figure 6. **Visualization of Coordinate Representations.** We illustrate the geometric relationships defined in Sec. 3.2. The canonical frame serves as a gravity-aligned local reference. Based on this frame, we visualize the spatio-temporally invariant relative transformations for the head, hands, and root orientation used to construct our model’s features.

A. Representation Visualization

We provide visual illustrations of the coordinate representations detailed in Sec. 3.2. Following EgoAllo [53], the canonical frame is defined as the projection of the head coordinate onto the ground plane, where the z -axis is aligned with gravity and y -axis aligns with the head’s forward direction. Figure 6 visualizes this canonical frame and other key coordinate representations (ΔT_t^{head} , T_t^{head} , $R_t^{\text{head} \rightarrow \text{cano}}$, h_t , ΔR_t^{cano} , R_t^{root}).

B. Augmentation Details

We present the detailed hyperparameters for the stochastic augmentation strategy introduced in Sec. 3.4. This method ensures realistic egocentric spatial and temporal variations.

Spatial Augmentation. To simulate diverse capture setups, ranging from monocular and stereo to fisheye systems with varying orientations (forward to downward), we sample spatial parameters uniformly. The sampling ranges are defined as follows (angles in radians):

$$\begin{aligned} \psi_x &\in [0.35, 2.15], \psi_y \in [0.35, 1.35] \\ \phi_x &\in [-0.15, 0.15], \phi_y \in [0.0, 1.5], p \in [2.0, 10.0] \end{aligned} \quad (12)$$

To preserve realistic aspect ratios and tilt orientations, we

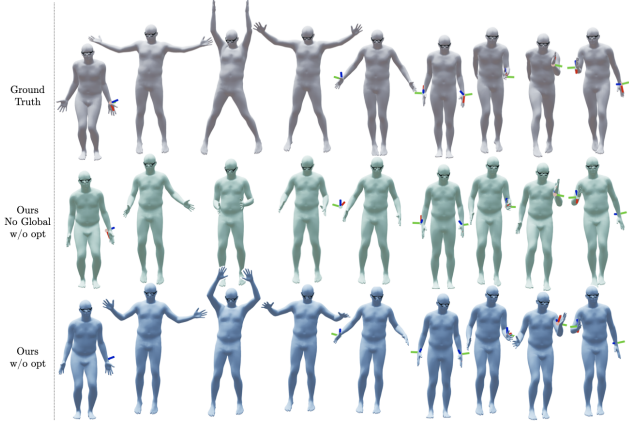


Figure 7. **Qualitative Results of Ablation Studies.** In a jumping and running sequence, the **No Global** model incorrectly places invisible hands within the visible zone due to the lack of global context. In contrast, our full model correctly infers that the invisible hands are outside the FoV.

enforce the constraints:

$$0.4 \leq \frac{\psi_y}{\psi_x} \leq 1.1, \quad \phi_y \leq 0.4 + (\psi_y - 0.35) \cdot 1.1. \quad (13)$$

Temporal Augmentation. We employ a two-stage stochastic process to model realistic burst errors, consisting of short-transient (e.g., motion blur) and long-drop (e.g., occlusion) modes. We avoid standard Bernoulli masking, as its implied Geometric distribution fails to capture prolonged signal losses, which are frequent in real-world egocentric videos. Furthermore, for robustness, we dynamically sample the occlusion ratio instead of using a fixed rate.

For a sequence of length T , the number of drop events K is sampled from a Poisson distribution $K \sim \text{Poisson}(\lambda)$. To ensure the total drop ratio matches our target rate ρ , we derive the Poisson parameter λ as:

$$\lambda = \frac{T \cdot \rho}{\mathbb{E}[D]} \quad (14)$$

, where $\mathbb{E}[D]$ is the expected duration of a single drop. The drop duration D is independently sampled from a heavy-tailed Log-Normal distribution, and the start index of each event is sampled uniformly. The specific parameters for each mode, defined by the Log-Normal’s mean $m = \mathbb{E}[D]$ and standard deviation s , are:

$$\begin{aligned} \text{Short: } \rho &\sim \mathcal{U}(0.00, 0.10), m = 2.0, s = 1.0 \\ \text{Long: } \rho &\sim \mathcal{U}(0.00, 0.20), m = 28.0, s = 25.0 \end{aligned} \quad (15)$$

The final visibility mask is formed by the union of these independent masks. For the long-drop mode, durations are clipped to a minimum of 5 frames.

C. Qualitative Results of Ablation Studies

Complementing the quantitative results in Sec. 4.4, Figure 7 visualizes the impact of the global context (\mathcal{G}). At the beginning of the motion, our full model correctly reconstructs the hands raised to the sides, whereas the **No Global** model incorrectly raises them in front of the body. After a few moments, the subject swings their arms forward, leading to the clear detection of wrists in the frontal view. Our full model is aware of this information via global context \mathcal{G} , allowing it to correctly infer that the previously missing hands were outside the FoV. However, the **No Global** model, limited by local attention and lacks global context, cannot access this sequence-level cue and thus generates the wrong motion. This implies that the global context implicitly encodes FoV information, which is crucial for accurately reconstructing egocentric body motion.

References

[1] Project aria. <https://www.projectaria.com/>, . 1, 2

[2] Ray-ban meta smart glasses. <https://www.meta.com/smart-glasses>, . 1, 2

[3] Rokoko smartsuit pro. <https://www.rokoko.com/products/smartsuit-pro>. 2

[4] Spectacles by snap inc. <https://www.spectacles.com/>. 1

[5] Vuzix smart glasses. <https://www.vuzix.com/pages/smart-glasses>. 1

[6] Xsens mvn link. <https://www.movella.com/products/motion-capture/xsens-mvn-link>. 2

[7] Sadegh Aliakbarian, Pashmina Cameron, Federica Bogo, Andrew Fitzgibbon, and Thomas J Cashman. Flag: Flow-based 3d avatar generation from sparse observations. In *CVPR*, 2022. 5

[8] Sadegh Aliakbarian, Fatemeh Saleh, David Collier, Pashmina Cameron, and Darren Cosker. Hmd-nemo: Online 3d avatar motion generation from sparse observations. In *ICCV*, 2023. 2

[9] German Barquero, Sergio Escalera, and Cristina Palmero. Seamless human motion composition with blended positional encodings. In *CVPR*, 2024. 2, 4

[10] Iz Beltagy, Matthew E. Peters, and Arman Cohan. Longformer: The long-document transformer. *arXiv preprint arXiv:2004.05150*, 2020. 4

[11] Angela Castillo, Maria Escobar, Guillaume Jeanneret, Albert Pumarola, Pablo Arbeláez, Ali Thabet, and Artsiom Sanakoyeu. Bodiffusion: Diffusing sparse observations for full-body human motion synthesis. In *ICCV*, 2023. 2, 8

[12] Seunggeun Chi, Pin-Hao Huang, Enna Sachdeva, Hengbo Ma, Karthik Ramani, and Kwonjoon Lee. Estimating ego-body pose from doubly sparse egocentric video data. In *NeurIPS*, 2024. 5

[13] Rishabh Dabral, Muhammad Hamza Mughal, Vladislav Golyanik, and Christian Theobalt. Mofusion: A framework for denoising-diffusion-based motion synthesis. In *CVPR*, 2023. 2

[14] Andrea Dittadi, Sebastian Dziadzio, Darren Cosker, Ben Lundell, Thomas J Cashman, and Jamie Shotton. Full-body motion from a single head-mounted device: Generating smpl poses from partial observations. In *ICCV*, 2021. 2

[15] Juechu Dong, Boyuan Feng, Driss Guessous, Yanbo Liang, and Horace He. Flex attention: A programming model for generating optimized attention kernels. *arXiv preprint arXiv:2412.05496*, 2024. 5

[16] Yuming Du, Robin Kips, Albert Pumarola, Sebastian Starke, Ali Thabet, and Artsiom Sanakoyeu. Avatars grow legs: Generating smooth human motion from sparse tracking inputs with diffusion model. In *CVPR*, 2023. 2

[17] Jakob Engel, Kiran Somasundaram, Michael Goesele, Albert Sun, Alexander Gumno, Andrew Turner, Arjang Talat-tor, Arnie Yuan, Bilal Souti, Brighid Meredith, Cheng Peng, Chris Sweeney, Cole Wilson, Dan Barnes, Daniel DeTone, David Caruso, Derek Valleroy, Dinesh Ginjupalli, Duncan Frost, Edward Miller, Elias Mueggler, Evgeniy Oleinik, Fan Zhang, Guruprasad Somasundaram, Gustavo Solaira, Harry Lanaras, Henry Howard-Jenkins, Huixuan Tang, Hyo Jin Kim, Jaime Rivera, Ji Luo, Jing Dong, Julian Straub, Kevin Bailey, Kevin Eckenhoff, Lingni Ma, Luis Pesqueira, Mark Schwesinger, Maurizio Monge, Nan Yang, Nick Charron, Nikhil Raina, Omkar Parkhi, Peter Borschowa, Pierre Moulou, Prince Gupta, Raul Mur-Artal, Robbie Pennington, Sachin Kulkarni, Sagar Miglani, Santosh Gondi, Saransh Solanki, Sean Diener, Shangyi Cheng, Simon Green, Steve Saarinen, Suvam Patra, Tassos Mourikis, Thomas Whelan, Tripti Singh, Vasileios Balntas, Vijay Baiyya, Wilson Dreewes, Xiaqing Pan, Yang Lou, Yipu Zhao, Yusuf Mansour, Yuyang Zou, Zhaoyang Lv, Zijian Wang, Mingfei Yan, Carl Ren, Renzo De Nardi, and Richard Newcombe. Project aria: A new tool for egocentric multi-modal ai research. *arXiv preprint arXiv:2308.13561*, 2023. 3

[18] Kristen Grauman, Andrew Westbury, Lorenzo Torresani, Kris Kitani, Jitendra Malik, Triantafyllos Afouras, Kumar Ashutosh, Vijay Baiyya, Siddhant Bansal, Bikram Boote, Eugene Byrne, Zach Chavis, Joya Chen, Feng Cheng, Fu-Jen Chu, Sean Crane, Avijit Dasgupta, Jing Dong, Maria Escobar, Cristhian Forigua, Abrham Gebreselasie, Sanjay Haresh, Jing Huang, Md Mohaiminul Islam, Suyog Jain, Rawal Khirodkar, Devansh Kukreja, Kevin J Liang, Jia-Wei Liu, Sagnik Majumder, Yongsen Mao, Miguel Martin, Effrosyni Mavroudi, Tushar Nagarajan, Francesco Ragusa, Santhosh Kumar Ramakrishnan, Luigi Seminara, Arjun Somayazulu, Yale Song, Shan Su, Zihui Xue, Edward Zhang, Jin Xu Zhang, Angela Castillo, Changan Chen, Xinzhu Fu, Ryosuke Furuta, Cristina Gonzalez, Prince Gupta, Jiabo Hu, Yifei Huang, Yiming Huang, Leslie Khoo, Anush Kumar, Robert Kuo, Sach Lakhavani, Miao Liu, Mi Luo, Zhengyi Luo, Brighid Meredith, Austin Miller, Oluwatumini Ogun-tola, Xiaqing Pan, Penny Peng, Shraman Pramanick, Merey Ramazanova, Fiona Ryan, Wei Shan, Kiran Somasundaram, Chenan Song, Audrey Southerland, Masatoshi Tateno, Huiyu Wang, Yuchen Wang, Takuma Yagi, Mingfei Yan, Xitong Yang, Zecheng Yu, Shengxin Cindy Zha, Chen Zhao, Zi-wei Zhao, Zhifan Zhu, Jeff Zhuo, Pablo Arbelaez, Gedas Bertasius, David Crandall, Dima Damen, Jakob Engel, Giovanni Maria Farinella, Antonino Furnari, Bernard Ghanem, Judy Hoffman, C. V. Jawahar, Richard Newcombe, Hyun Soo Park, James M. Rehg, Yoichi Sato, Manolis Savva, Jianbo Shi, Mike Zheng Shou, and Michael Wray. Ego-exo4d: Understanding skilled human activity from first- and third-person perspectives. In *CVPR*, 2024. 4, 5

[19] Vladimir Guzov, Aymen Mir, Torsten Sattler, and Gerard Pons-Moll. Human poseitioning system (hps): 3d human pose estimation and self-localization in large scenes from body-mounted sensors. In *CVPR*, 2021. 2

[20] Vladimir Guzov, Yifeng Jiang, Fangzhou Hong, Gerard Pons-Moll, Richard Newcombe, C. Karen Liu, Yuting Ye, and Lingni Ma. Hmd²: Environment-aware motion generation from single egocentric head-mounted device. In *3DV*, 2025. 1, 2

[21] Jonathan Ho, Ajay Jain, and Pieter Abbeel. Denoising diffusion probabilistic models. In *NeurIPS*, 2020. 3, 4, 5

[22] Yinghao Huang, Manuel Kaufmann, Emre Aksan, Michael J. Black, Otmar Hilliges, and Gerard Pons-Moll. Deep inertial poser learning to reconstruct human pose from sparse inertial measurements in real time. *ACM TOG*, 2018. 2

[23] Albert Q. Jiang, Alexandre Sablayrolles, Arthur Mensch, Chris Bamford, Devendra Singh Chaplot, Diego de las Casas, Florian Bressand, Gianna Lengyel, Guillaume Lample, Lucile Saulnier, Lélio Renard Lavaud, Marie-Anne Lachaux, Pierre Stock, Teven Le Scao, Thibaut Lavril, Thomas Wang, Timothée Lacroix, and William El Sayed. Mistral 7b. *arXiv preprint arXiv:2310.06825*, 2023. 4

[24] Chiyu Max Jiang, Andre Cornman, Cheolho Park, Ben Sapp, Yin Zhou, and Dragomir Anguelov. Motiondiffuser: Controllable multi-agent motion prediction using diffusion. In *CVPR*, 2023. 2

[25] Hao Jiang and Kristen Grauman. Seeing invisible poses: Estimating 3d body pose from egocentric video. In *CVPR*, 2017. 2

[26] Hao Jiang and Vamsi Krishna Ithapu. Egocentric pose estimation from human vision span. In *ICCV*, 2021. 2

[27] Jiaxi Jiang, Paul Streli, Huajian Qiu, Andreas Fender, Larissa Laich, Patrick Snape, and Christian Holz. Avataposer: Articulated full-body pose tracking from sparse motion sensing. In *ECCV*, 2022. 2, 3, 4, 5

[28] Jiaxi Jiang, Paul Streli, Manuel Meier, and Christian Holz. Egoposer: Robust real-time egocentric pose estimation from sparse and intermittent observations everywhere. In *ECCV*, 2024. 2, 4, 5, 7

[29] Yifeng Jiang, Yuting Ye, Deepak Gopinath, Jungdam Won, Alexander W Winkler, and C Karen Liu. Transformer inertial poser: Real-time human motion reconstruction from sparse imus with simultaneous terrain generation. In *SIGGRAPH Asia*, 2022. 2

[30] Jiye Lee and Hanbyul Joo. Mocap everyone everywhere: Lightweight motion capture with smartwatches and a head-mounted camera. In *CVPR*, 2024. 1, 2, 3

[31] Juho Lee, Yoonho Lee, Jungtaek Kim, Adam R. Kosiorek, Seungjin Choi, and Yee Whye Teh. Set transformer: A framework for attention-based permutation-invariant neural networks. In *Proc. ICML*, 2019. 4

[32] Jiaman Li, Karen Liu, and Jiajun Wu. Ego-body pose estimation via ego-head pose estimation. In *CVPR*, 2023. 1, 2, 3, 8

[33] Jiefeng Li, Jinkun Cao, Haotian Zhang, Davis Rempe, Jan Kautz, Umar Iqbal, and Ye Yuan. Gemmo: Generative models for human motion synthesis. In *ICCV*, 2025. 2, 4

[34] Zhengyi Luo, Ryo Hachiuma, Ye Yuan, and Kris Kitani. Dynamics-regulated kinematic policy for egocentric pose estimation. In *NeurIPS*, 2021. 2

[35] Lingni Ma, Yuting Ye, Fangzhou Hong, Vladimir Guzov, Yifeng Jiang, Rowan Postyeni, Luis Pesqueira, Alexander Ghami, Vijay Baiyya, Hyo Jin Kim, Kevin Bailey, David Soriani Fosas, C. Karen Liu, Ziwei Liu, Jakob Engel, Renzo De Nardi, and Richard Newcombe. Nymeria: A massive collection of multimodal egocentric daily motion in the wild. In *ECCV*, 2024. 4

[36] Naureen Mahmood, Nima Ghorbani, Nikolaus F. Troje, Gerard Pons-Moll, and Michael J. Black. Amass: Archive of motion capture as surface shapes. In *ICCV*, 2019. 4, 5

[37] Josh Merel, Saran Tunyasuvunakool, Arun Ahuja, Yuval Tassa, Leonard Hasenclever, Vu Pham, Tom Erez, Greg Wayne, and Nicolas Heess. Catch & carry: reusable neural controllers for vision-guided whole-body tasks. *ACM TOG*, 2020. 2

[38] Chaitanya Patel, Hiroki Nakamura, Yuta Kyuragi, Kazuki Kozuka, Juan Carlos Niebles, and Ehsan Adeli. Uniegomotion: A unified model for egocentric motion reconstruction, forecasting, and generation. In *ICCV*, 2025. 1, 2, 3, 8

[39] William Peebles and Saining Xie. Scalable diffusion models with transformers. In *ICCV*, 2023. 3, 4

[40] Luis Pineda, Taosha Fan, Maurizio Monge, Shobha Venkataraman, Paloma Sodhi, Ricky TQ Chen, Joseph Ortiz, Daniel DeTone, Austin Wang, Stuart Anderson, Jing Dong, Brandon Amos, and Mustafa Mukadam. Theseus: A library for differentiable nonlinear optimization. In *NeurIPS*, 2022. 5

[41] Davis Rempe, Tolga Birdal, Aaron Hertzmann, Jimei Yang, Srinath Sridhar, and Leonidas J. Guibas. Humor: 3d human motion model for robust pose estimation. In *ICCV*, 2021. 5

[42] Javier Romero, Dimitrios Tzionas, and Michael J. Black. Embodied hands: modeling and capturing hands and bodies together. *ACM TOG*, 2017. 3

[43] Jiaming Song, Chenlin Meng, and Stefano Ermon. Denoising diffusion implicit models. In *Proc. ICLR*, 2021. 5

[44] Jianlin Su, Murtadha Ahmed, Yu Lu, Shengfeng Pan, Wen Bo, and Yunfeng Liu. Roformer: Enhanced transformer with rotary position embedding. *Neurocomputing*, 2024. 4

[45] Guy Tevet, Sigal Raab, Brian Gordon, Yoni Shafir, Daniel Cohen-or, and Amit Haim Bermano. Human motion diffusion model. In *Proc. ICLR*, 2023. 2, 5

[46] Denis Tome, Patrick Peluse, Lourdes Agapito, and Hernan Badino. xr-egopose: Egocentric 3d human pose from an hmd camera. In *ICCV*, 2019. 2

[47] Denis Tome, Thimo Alldieck, Patrick Peluse, Gerard Pons-Moll, Lourdes Agapito, Hernan Badino, and Fernando De la Torre. Selfpose: 3d egocentric pose estimation from a headset mounted camera. *IEEE TPAMI*, 2020. 2

[48] Ashish Vaswani, Noam Shazeer, Niki Parmar, Jakob Uszkoreit, Llion Jones, Aidan N Gomez, Łukasz Kaiser, and Illia Polosukhin. Attention is all you need. In *NeurIPS*, 2017. 4

[49] Timo Von Marcard, Bodo Rosenhahn, Michael J Black, and Gerard Pons-Moll. Sparse inertial poser: Automatic 3d human pose estimation from sparse imus. In *Comput. Graph. Forum*, 2017. 2

[50] Jian Wang, Lingjie Liu, Weipeng Xu, Kripasindhu Sarkar, and Christian Theobalt. Estimating egocentric 3d human pose in global space. In *ICCV*, 2021. 2

[51] Jian Wang, Diogo Luvizon, Weipeng Xu, Lingjie Liu, Kripasindhu Sarkar, and Christian Theobalt. Scene-aware egocentric 3d human pose estimation. In *CVPR*, 2023.

[52] Weipeng Xu, Avishek Chatterjee, Michael Zollhoefer, Helge Rhodin, Pascal Fua, Hans-Peter Seidel, and Christian Theobalt. Mo 2 cap 2: Real-time mobile 3d motion capture with a cap-mounted fisheye camera. *IEEE TVCG*, 2019. 2

- [53] Brent Yi, Vickie Ye, Maya Zheng, Yunqi Li, Lea Müller, Georgios Pavlakos, Yi Ma, Jitendra Malik, and Angjoo Kanazawa. Estimating body and hand motion in an ego-sensed world. In *CVPR*, 2025. [1](#), [2](#), [3](#), [4](#), [6](#), [8](#), [9](#)
- [54] Xinyu Yi, Yuxiao Zhou, and Feng Xu. Transpose: Real-time 3d human translation and pose estimation with six inertial sensors. *ACM TOG*, 2021. [2](#)
- [55] Xinyu Yi, Yuxiao Zhou, Marc Habermann, Soshi Shimada, Vladislav Golyanik, Christian Theobalt, and Feng Xu. Physical inertial poser (pip): Physics-aware real-time human motion tracking from sparse inertial sensors. In *CVPR*, 2022.
- [56] Xinyu Yi, Yuxiao Zhou, Marc Habermann, Vladislav Golyanik, Shaohua Pan, Christian Theobalt, and Feng Xu. Egolocate: Real-time motion capture, localization, and mapping with sparse body-mounted sensors. *ACM TOG*, 2023. [2](#)
- [57] Xinyu Yi, Yuxiao Zhou, and Feng Xu. Physical non-inertial poser (pnp): Modeling non-inertial effects in sparse-inertial human motion capture. In *SIGGRAPH*, 2024. [2](#)
- [58] Ye Yuan and Kris Kitani. 3d ego-pose estimation via imitation learning. In *ECCV*, 2018. [2](#)
- [59] Ye Yuan and Kris Kitani. Ego-pose estimation and forecasting as real-time pd control. In *ICCV*, 2019. [2](#)
- [60] Mingyuan Zhang, Zhongang Cai, Liang Pan, Fangzhou Hong, Xinying Guo, Lei Yang, and Ziwei Liu. Motiondiffuse: Text-driven human motion generation with diffusion model. *IEEE TPAMI*, 2024. [2](#)